Applied Physics Express **9**, 025101 (2016)
http://doi.org/**10.7567/APEX.9.025101**

Tunable waveguide bends with graphene-based anisotropic metamaterials

Zhao-xian Chen[1,2], Ze-guo Chen[1], Yang Ming[2], Ying Wu[1]*, and Yan-qing Lu[2]*

[1]*Division of Computer, Electrical and Mathematical Sciences and Engineering, King Abdullah University of Science and Technology (KAUST), Thuwal 23955-6900, Saudi Arabia*
[2]*National Laboratory of Solid State Microstructures and College of Engineering and Applied Sciences, Nanjing University, Nanjing 210093, P. R. China*

*E-mail: ying.wu@kaust.edu.sa; yqlu@nju.edu.cn

Received November 30, 2015; accepted December 20, 2015; published online January 15, 2016

We design tunable waveguide bends filled with graphene-based anisotropic metamaterials to achieve a nearly perfect bending effect. The anisotropic properties of the metamaterials can be described by the effective medium theory. The nearly perfect bending effect is demonstrated by finite element simulations of various structures with different bending curvatures and shapes. This effect is attributed to zero effective permittivity along the direction of propagation and matched effective impedance at the interfaces between the bending part and the dielectric waveguides. We envisage that the design will be applicable in the far-infrared and terahertz frequency ranges owing to the tunable dielectric responses of graphene.

Waveguide bends are necessary for photonic integration and are central to electromagnetic wave communication and manipulation. Conventional waveguide bends usually suffer from low transmission or serious wavefront distortion. Many solutions, such as plasmonic bends[1)] and photonic crystal bends,[2)] have been proposed to improve the bending performance of waveguides. In recent years, with the development of metamaterials, arbitrary waveguide bends were proposed under the framework of transformation optics[3)] and geometric optics.[4)] A 90° bend structure was realized experimentally with gradient index and isotropic metamaterials.[5)] Han and coworkers successfully designed adaptive waveguide bends with homogeneous, isotropic materials.[6)] Luo et al. proposed the so-called perfect bending waveguide based on realizable anisotropic epsilon-near-zero metamaterials.[7)] This waveguide was experimentally verified in the microwave region by Ma et al.[8)] Harnessing both zero-phase variation and uniform field-distribution properties, zero-index metamaterials with deliberately engineered defects are powerful for tunneling,[9,10)] total reflection or total transmission.[11,12)] Recently, anisotropic zero-index metamaterials have also been shown to be capable of arbitrarily manipulating the energy flux.[13,14)]

However, existing bends and zero-index metamaterials are universally challenged by their lack of adjustability and are limited by their applicable frequency range. For example, metamaterials made of split-ring resonators[8)] or I-shaped unit cells[5)] are sensitive to the wavelength and are difficult to extend to the high-frequency band. Fortunately, the use of graphene may help to resolve these issues because graphene has been shown to have high carrier mobility and feasible tunability[15,16)] with electric gating or doping in the electromagnetic regime. Graphene was previously used in field transistors,[17)] wave modulators,[18)] polarizers,[19)] absorbers,[20)] and sensors.[21,22)] For example, we have recently reported an enhanced light-graphene interaction platform by combing graphene with lab-on-a-rod techniques.[19)] Alternately aligned graphene and metal gratings were designed to achieve Fano-type resonance by exploiting their different responses to electromagnetic waves.[22)] Furthermore, metamaterials based on graphene/dielectric multilayers have also been studied both theoretically[23,24)] and experimentally.[25,26)] The strong coupling between the surface plasmon polaritons in graphene sheets makes graphene a powerful material for controlling wave radiation[27)] and for designing ultrasensitive modulators.[28)] Properly designed graphene-based metamaterials should also be beneficial in bending electromagnetic waves as desired.

In this Letter, we propose tunable waveguide bends using a graphene-based anisotropic metamaterial (GBAM) made of graphene layers that are alternately stacked between dielectric layers. We use the effective medium theory to understand the anisotropic dielectric property of GBAM. Nearly perfect bending is achieved by tuning graphene's Fermi level to realize zero index along the propagation direction. Our structure is applicable to different periods of GBAM and to different bending shapes. Using GBAM, we can arbitrarily guide and bend electromagnetic waves over a large frequency range, these are properties that are promising for applications in telecommunications and photonics.

A schematic of a two-dimensional (2D) bend is presented in Fig. 1(a). Regions 1 and 3 are dielectric waveguides with relative permittivity, ε_d. Region 2 is our designed GBAM made of multiple concentric layers of periodically altered dielectric and graphene with the radial direction normal to the surfaces of the layers. This GBAM is sandwiched between two metal layers that can serve as parallel electrodes to uniformly bias the chemical potential of graphene. In the far-infrared and terahertz regimes, these metal walls can be regarded as a perfect metal and the perfect conducting condition is therefore employed. If the metal boundaries are replaced by a low-index dielectric medium, the functionality of the electrodes will be disabled and the wave field will be diffracted, penetrating into the walls of the waveguides so that it will not be possible to achieve a perfect bending effect. The GBAM between the metal walls can be treated as a uniform medium whose permittivity tensor is expressed as $[\varepsilon_r, \varepsilon_\theta, \varepsilon_z]$ in cylindrical coordinates, with the subscripts r, θ, and z denoting the radial, azimuthal, and z-axes, respectively. The inner and outer radii of the bend are r_1 and r_2, respectively. We assume that there is a transverse magnetic (TM) wave incident from Region 1, i.e., the magnetic field $\vec{H} = (0, 0, H_z)$ is along the z-axis. No magnetic effect is considered here, and all regions have isotropic permeability, μ_0. According to Maxwell's equations, fields in Region 2 obey the following relationship:

$$\varepsilon_r \frac{\partial E_r}{\partial t} = \frac{1}{r}\frac{\partial H_z}{\partial \theta}, \quad \varepsilon_\theta \frac{\partial E_\theta}{\partial t} = \frac{\partial H_z}{\partial r}. \tag{1}$$

Thus, we could infer that when ε_θ is zero, H_z should be a constant along the radial direction and a TM wavefront remains

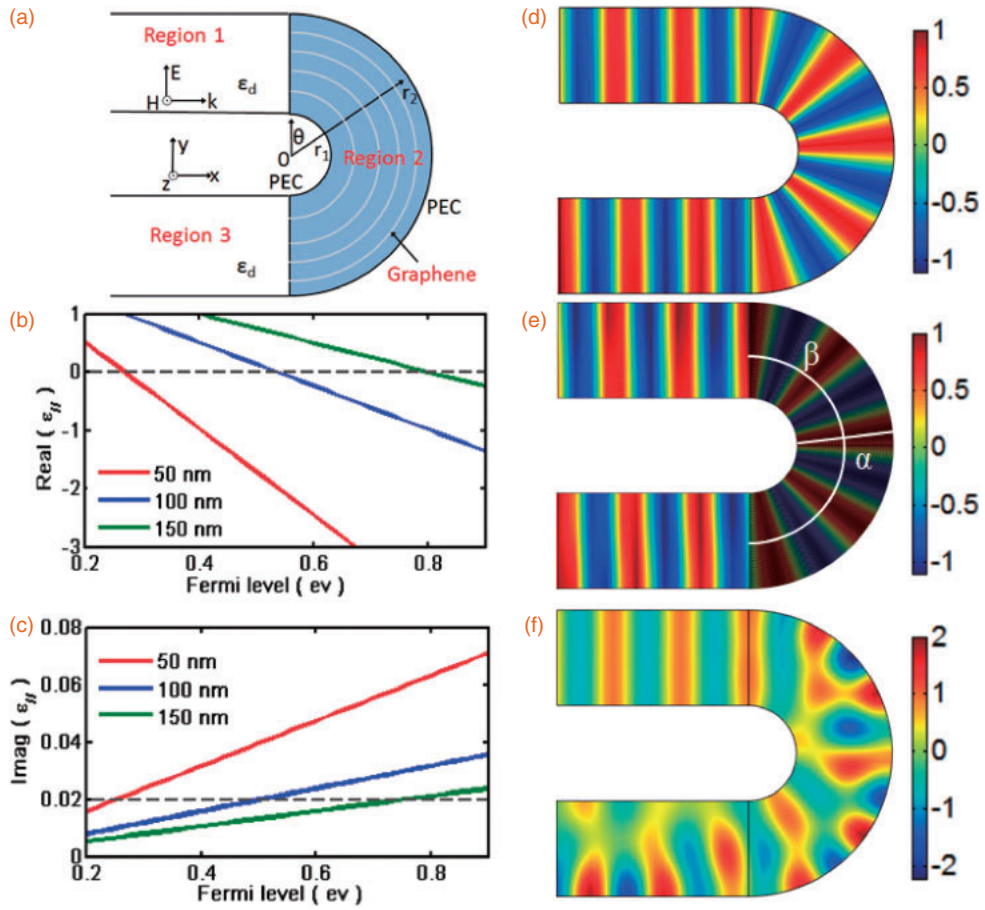

Fig. 1. (a) Schematic diagram of the bend. A TM wave is launched from Region 1 with the magnetic field H along the z-axis. Regions 1 and 3 are metallic waveguides filled with the dielectric of ε_d. Region 2 is made of GBAM and the gray curves represent graphene layers equally spaced between dielectric layers, ε_d, with the thickness t_d (not proportionate to the real design). (b, c) Real and imaginary parts of GBAM's $\varepsilon_{||}$ for different t_d values and Fermi levels, respectively. Other parameters are $\lambda_0 = 10\,\mu m$, $\Gamma = 0.1$ meV, and $\varepsilon_d = 2$. Black dashed lines signify $\mathrm{Re}\,\varepsilon_{||} = 0$ and $\mathrm{Im}\,\varepsilon_{||} = 0.02$. (d–f) Magnetic field distributions in a 180° bend filled with anisotropic dielectric ($\varepsilon_\theta = 0$ and $\varepsilon_r = 2$), GBAM, and isotropic dielectric ($\varepsilon = 2$), respectively. $\lambda_0 = 10\,\mu m$, $r_1 = 5\,\mu m$, and $r_2 = r_1 + \lambda_0$. For the GBAM in (e), the period is 100 nm and the Fermi level is 0.53 eV. α and β are curves in the radial and azimuthal directions with $\theta = 85°$ and $r = 10\,\mu m$, respectively.

in the bending process. Besides, if the radial component of the permittivity tensor, ε_r, equals ε_d, the wave impedances of the three regions match (i.e., $\sqrt{\mu_0/\varepsilon_r} = \sqrt{\mu_0/\varepsilon_d}$) and the reflection at the interfaces between different regions vanishes. We performed numerical simulations with COMSOL Multiphysics (a commercial software based on the finite-element method) to validate the bending effect of this anisotropic material. As a proof of concept, we set $\varepsilon_\theta = 0$, $\varepsilon_r = \varepsilon_d = 2$ and chose the vacuum wavelength $\lambda_0 = 10\,\mu m$, which is approximately the working wavelength of a CO_2 laser. The magnetic field distribution inside such a waveguide bend is shown in Fig. 1(d), where a perfect bending effect without any wavefront distortion can be seen.

For our proposed GBAM, the dielectric spacers have the thickness t_d and also the same permittivity ε_d as the waveguide materials. In the far-infrared and terahertz regions, where the photon energy is much lower than graphene's biased Fermi level E_f, only the intraband electron transition is dominant and graphene's surface conductivity can be simplified to $\sigma_g = ie^2E_f/[\pi\hbar(\hbar\omega + i2\Gamma)]$, where e is the electron charge, E_f is the Fermi level, Γ is the intrinsic loss, and ω is the angular frequency of the incident wave.[29] To approximate the GBAM as an effective medium, the graphene is treated as a dielectric layer with a very small thickness of $t_g = 1$ nm, and its permittivity is derived from $\varepsilon_g = \varepsilon_0 + i\sigma_g/(\omega t_g)$, where ε_0 is the vacuum permittivity.[30] When the thickness of the spacer, t_d, is much smaller than the considered wavelength, the effective permittivity tensor of the GBAM can be determined by the following effective medium theory:[31]

$$\varepsilon_\perp = \varepsilon_r = \frac{\varepsilon_g\varepsilon_d(t_g + t_d)}{t_g\varepsilon_d + t_d\varepsilon_g},$$
$$\varepsilon_{||} = \varepsilon_\theta = \varepsilon_z = \frac{t_g\varepsilon_g + t_d\varepsilon_d}{t_g + t_d}. \quad (2)$$

From Eq. (2), we see that ε_r approximately equals ε_d when the spacer thickness t_d is considerably larger than t_g, meaning that ε_r will not be affected by graphene's properties and the impedance-matching condition is satisfied. On the other hand, ε_θ is tunable when the Fermi level or periodicity of graphene changes. We plot the real [Fig. 1(b)] and imaginary [Fig. 1(c)] parts of ε_θ versus E_f for various t_d values. Here, we again set $\varepsilon_d = 2$ and $\lambda_0 = 10\,\mu m$. The dashed line in Fig. 1(b) signifies the zero line of the real part of ε_θ. We observe that the larger the period, the higher the Fermi level required for $\mathrm{Re}\,\varepsilon_\theta = 0$. We also find that the required Fermi levels are much higher than the photon energy ($E \approx 0.12$ eV), which justifies our calculation of graphene's conductivity by

ignoring the interband electron transition. When $\mathrm{Re}\,\varepsilon_\theta = 0$, the corresponding imaginary parts of ε_θ for different periods are all about 0.02, shown as the dashed line in Fig. 1(c). This means that metamaterials' dissipation is similar for different period and Fermi level combinations.

We further perform numerical simulations to verify the validity of using GBAM to achieve the perfect bending effect. We set the width of the bending waveguide to $r_2 - r_1 = \lambda_0$ and assume that $r_1 = 5\,\mu\mathrm{m}$ is the inner radius of the bend. The dielectric/graphene period in the GBAM is chosen to be 100 nm, and the magnetic field amplitude of the TM incidence is set at 1 A/m. The outer metallic boundaries of the GBAM can be simply treated as perfect electric boundaries in the simulation considering the metal's relatively low dissipation in the far-infrared and terahertz ranges. As shown in Fig. 1(e), near-perfect 180° bending is achieved when $E_\mathrm{f} = 0.53\,\mathrm{eV}$ at which $\varepsilon_\theta \approx 0$. Compared with Fig. 1(d), the shape of the wavefront is well preserved in the bend, and there is almost no reflection across the interfaces on the GBAM. This result confirms that GBAM behaves exactly like a homogeneous, anisotropic medium with $\varepsilon_\theta = 0$ and $\varepsilon_\mathrm{r} = 2$ when the Fermi level of graphene is properly tuned. By contrast, Fig. 1(f) shows the field distribution for the same incident wave but with the GBAM replaced by the isotropic dielectric. A significant wavefront distortion is observed.

To better understand the mechanism of the perfect bending effect with GBAM, we select two curves along the radial and azimuthal directions in the bending region, marked as α and β in Fig. 1(e), and plot the magnetic field distributions. According to Eq. (1), a uniform magnetic field distribution along curve α is expected when $\varepsilon_\theta = 0$. Figure 2(a) verifies this conclusion by showing that the magnitude of H_z is about 0.95 A/m, together with many sharp peaks. In the vicinity of the graphene sheets, Ampere's law is written as

$$\varepsilon_\theta \frac{\partial E_\theta}{\partial t} + J_\theta = \frac{\partial H_z}{\partial r}, \tag{3}$$

where J_θ is the surface current on graphene induced by the plasmon resonance. As a result, sharp changes in magnetic field are observed near the surface of the graphene, as exhibited in the inset of Fig. 2(a).

The plasmonic effect is also apparent in Fig. 2(b), where the small oscillations are induced by interference between the incident wave and the plasmonic wave of the graphene. We can exactly calculate the wave vector of the surface plasmon polariton of the graphene using

$$k_\mathrm{SPP} = k_0 \sqrt{\varepsilon_\mathrm{d} + \left(\frac{2i\varepsilon_\mathrm{d}}{\eta_0 \sigma_\mathrm{g}}\right)^2}. \tag{4}$$

Here, η_0 is the intrinsic impedance of free space.[27] The wavelength of the graphene plasmon is thus $\lambda_\mathrm{SPP} = 2\pi/\mathrm{Re}\,k_\mathrm{SPP} \approx 0.31\,\mu\mathrm{m}$, which matches the interference pattern in Fig. 2(b) well. The EM wave suffers propagation loss in the bending process as the amplitude of the magnetic field decreases from 1 to 0.9 A/m along the azimuthal direction. Since we can obtain $\mathrm{Im}\,k_\mathrm{SPP} \propto \varepsilon_\mathrm{d}$ from Eq. (4), a dielectric with smaller ε_d is preferred to reduce the bending dissipation.

In Fig. 2(c), we plot the Fermi levels [calculated using Eq. (2)] that are needed to obtain $\mathrm{Re}\,\varepsilon_\theta = 0$ with different periods as the blue curve. This figure shows that a larger period requires a higher Fermi level. For each period, we also perform numerical simulations by tuning the Fermi level of the graphene layers to achieve the perfect bending effect, i.e., a uniform magnetic field distribution along the radial direction in GBAM and no wavefront distortion. These results are plotted in Fig. 2(c) (red dots); they are in excellent agreement with the prediction of Eq. (2), confirming that the effective medium theory is able to describe GBAM.

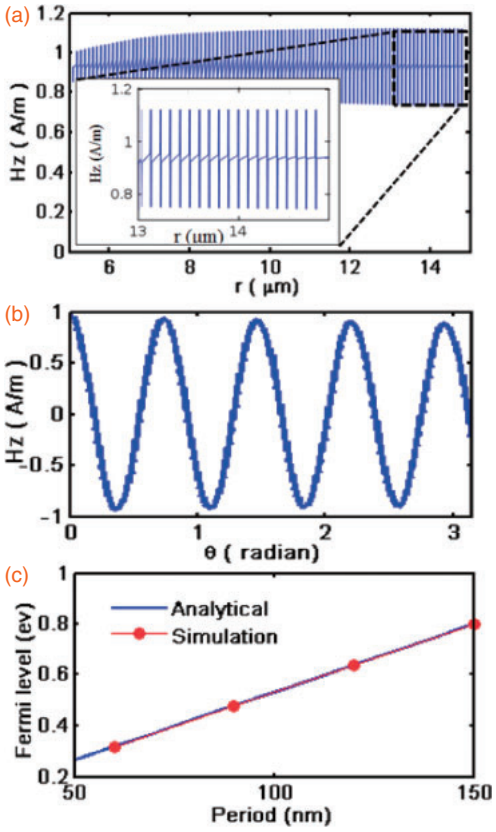

Fig. 2. (a, b) Magnetic field distributions at curves α and β marked in Fig. 1(e), respectively. (c) Fermi level required for $\varepsilon_\theta = 0$. Results of the analytical calculations (blue line) match those of the numerical simulations (red dots) well.

Here, a perfect bending effect with GBAM is successfully demonstrated, and the validity of the effective medium theory in describing the anisotropic properties of the metamaterials is verified. In what follows, we study the tunability of the bend as well as the performance characteristics of bends with different bending curvatures and shapes. First, the adjustability of graphene's permittivity permits the application of our GBAM bending structure within a large frequency regime. We calculate the Fermi level required for $\varepsilon_\theta = 0$ with different periods and frequencies. As shown in Fig. 3(a), the working frequency of the GBAM bend can be extended from the far-infrared to the terahertz region as long as we change the Fermi level of graphene within a reasonable range.[32] For a given structure (period), it is possible to guide the wave perfectly by changing the Fermi level to achieve the required effective medium profile of the GBAM at different frequencies. Theoretically, we could arbitrarily guide the incident wave with GBAM without energy reflection or wavefront distortion as long as we keep $\varepsilon_\theta = 0$ by tuning graphene's Fermi level.

The effect of the bend curvature is next studied by changing the inner radius r_1. Transmissivity versus r_1 is

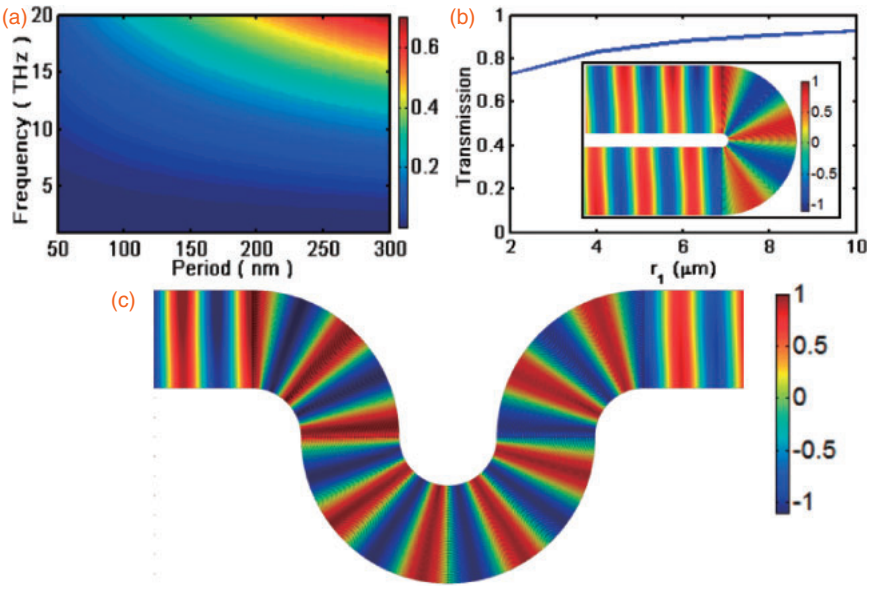

Fig. 3. (a) Fermi levels required for $\varepsilon_{||} = 0$ at different periods and frequencies. The unit of the colorbar is eV. (b) Transmittances of 180° bending at different r_1 values. The inset shows the magnetic field distribution when $r_1 = 2\,\mu m$. Other parameters are the same as those used in Fig. 1(e). (c) Magnetic field distribution in 360° bending filled with GBAM. Other parameters are the same as those used in Fig. 1(e).

plotted in Fig. 3(b). Although the transmissivity slightly decreases when we maintain the waveguide width and reduce r_1, a perfect bending functionality of GBAM persists, as shown in the inset, with $r_1 = 2\,\mu m$. A larger curvature results in a stronger surface current dissipation on graphene, which accounts for the decrease in transmissivity. In Fig. 3(c), we further simulate 360° bending when other parameters are the same as those in the case shown in Fig. 1(e). The wavefront remains well preserved after transmitting through the bending waveguide.

In conclusion, we proposed perfect bending of TM waves using graphene-based anisotropic metamaterials made of multiple concentric layers of graphene and dielectric. Tuning graphene's Fermi level can give rise to zero effective index along the propagation direction such that the TM wavefront is preserved and the perfect bending effect is achieved. We investigated the magnetic field distributions to validate bending functionality. The exceptional elasticity and flexible tunability of graphene's electric response enable the design of bends with different curvatures, shapes, and frequency ranges.

Acknowledgments The work described in this paper was supported by King Abdullah University of Science and Technology (KAUST), the National Science Foundation of China (NSFC) under contact No. 61225026, and the Program for Changjiang Scholars and Innovative Research Teams at the University under contract IRT13021.

1) G. Veronis and S. Fan, Appl. Phys. Lett. **87**, 131102 (2005).
2) A. Mekis, J. C. Chen, I. Kurland, S. Fan, P. R. Villeneuve, and J. D. Joannopoulos, Phys. Rev. Lett. **77**, 3787 (1996).
3) W. Jiang, T. Cui, X. Zhou, X. Yang, and Q. Cheng, Phys. Rev. E **78**, 066607 (2008).
4) Z. L. Mei and T. J. Cui, J. Appl. Phys. **105**, 104913 (2009).
5) Z. L. Mei and T. J. Cui, Opt. Express **17**, 18354 (2009).
6) T. Han, C.-W. Qiu, and X. Tang, Opt. Lett. **36**, 181 (2011).
7) J. Luo, P. Xu, H. Chen, B. Hou, L. Gao, and Y. Lai, Appl. Phys. Lett. **100**, 221903 (2012).
8) H. F. Ma, J. H. Shi, W. X. Jiang, and T. J. Cui, Appl. Phys. Lett. **101**, 253513 (2012).
9) M. Silveirinha and N. Engheta, Phys. Rev. Lett. **97**, 157403 (2006).
10) B. Edwards, A. Alù, M. Young, M. Silveirinha, and N. Engheta, Phys. Rev. Lett. **100**, 033903 (2008).
11) V. Nguyen, L. Chen, and K. Halterman, Phys. Rev. Lett. **105**, 233908 (2010).
12) Y. Wu and J. Li, Appl. Phys. Lett. **102**, 183105 (2013).
13) J. Luo, W. Lu, Z. Hang, H. Chen, B. Hou, Y. Lai, and C. T. Chan, Phys. Rev. Lett. **112**, 073903 (2014).
14) J. Luo and Y. Lai, Sci. Rep. **4**, 5875 (2014).
15) F. Xia, H. Wang, D. Xiao, M. Dubey, and A. Ramasubramaniam, Nat. Photonics **8**, 899 (2014).
16) L. Ju, B. Geng, J. Horng, C. Girit, M. Martin, Z. Hao, H. A. Bechtel, X. Liang, A. Zettl, Y. R. Shen, and F. Wang, Nat. Nanotechnol. **6**, 630 (2011).
17) P. B. Bennett, Z. Pedramrazi, A. Madani, Y.-C. Chen, D. G. de Oteyza, C. Chen, F. R. Fischer, M. F. Crommie, and J. Bokor, Appl. Phys. Lett. **103**, 253114 (2013).
18) X. Gan, R.-J. Shiue, Y. Gao, K. F. Mak, X. Yao, L. Li, A. Szep, D. Walker, J. Hone, T. F. Heinz, and D. Englund, Nano Lett. **13**, 691 (2013).
19) J. Kou, J. Chen, Y. Chen, F. Xu, and Y. Lu, Optica **1**, 307 (2014).
20) R. Alaee, M. Farhat, C. Rockstuhl, and F. Lederer, Opt. Express **20**, 28017 (2012).
21) A. Davoyan, V. Popov, and S. Nikitov, Phys. Rev. Lett. **108**, 127401 (2012).
22) Z. Chen, J. Chen, Z. Wu, W. Hu, X. Zhang, and Y. Lu, Appl. Phys. Lett. **104**, 161114 (2014).
23) M. A. K. Othman, C. Guclu, and F. Capolino, J. Nanophotonics **7**, 073089 (2013).
24) A. Andryieuski, A. Lavrinenko, and D. Chigrin, Phys. Rev. B **86**, 121108 (2012).
25) H. Yan, X. Li, B. Chandra, G. Tulevski, Y. Wu, M. Freitag, W. Zhu, P. Avouris, and F. Xia, Nat. Nanotechnol. **7**, 330 (2012).
26) Z. Xu, C. Chen, S. Q. Y. Wu, B. Wang, J. Teng, C. Zhang, and Q. Bao, Proc. SPIE **8923**, 89230C (2013).
27) B. Wang, X. Zhang, F. García-Vidal, X. Yuan, and J. Teng, Phys. Rev. Lett. **109**, 073901 (2012).
28) I. Khromova, A. Andryieuski, and A. Lavrinenko, Laser Photonics Rev. **8**, 916 (2014).
29) A. Vakil and N. Engheta, Science **332**, 1291 (2011).
30) A. H. Castro Neto, F. Guinea, N. M. R. Peres, K. S. Novoselov, and A. K. Geim, Rev. Mod. Phys. **81**, 109 (2009).
31) C. Argyropoulos, N. M. Estakhri, F. Monticone, and A. Alù, Opt. Express **21**, 15037 (2013).
32) P.-Y. Chen and A. Alù, ACS Nano **5**, 5855 (2011).